*Stanford Exploration Project, Report 108, April 29, 2001, pages 1–**??***

Amplitude analysis in the angle domain

Douglas Gratwick[1]

ABSTRACT

This paper discusses amplitude vs. angle (AVA) analysis using image gathers generated from a wave-equation migration algorithm. An AVA cross-plot muting algorithm is used to highlight parts of an image corresponding to a Class III, low impedance, AVO sand. Processing to eliminate surface multiples is used on the synthetic data, thereby enhancing reflectors. Results show that our AVA muting algorithm is effective for both a synthetic and a real dataset.

INTRODUCTION

Amplitude variation with offset, AVO, has become an essential tool in the petroleum industry for hydrocarbon detection (Rutherford and Williams, 1989). AVO responses vary depending on the physical parameters of the reflection interface and incidence angle (Shuey, 1985). In relatively simple geologic settings, offset is a simple function of angle (Castagna and Smith, 1994). However, a more realistic $V(z,\mathbf{m})$ will make offset and incidence angle a complex relation (Sheriff, 1995). In these settings, amplitude variation with angle (AVA) is a preferable alternative to AVO analysis.

Wave equation migration methods generally provide for easy angle domain image gather extraction (Prucha et al., 1999). The gathers from wave equation methods are in depth and offset ray parameter. The details of the angle domain image gather extraction will be discussed in this paper. The models chosen for this study are relatively simple, with flat layers allowing for a direct comparison between offset ray parameter and angle. However, the presence of a salt body caused complex wave propagation. The resultant triplication and multi-pathing is generally handled well by wave equation migration methods (Biondi, 2000), and this is the migration method used in our study.

The attribute chosen for our AVA analysis is the intercept*gradient (A*B) attribute, which is commonly used in the petroleum industry (Castagna et al., 1998). Typical Gulf of Mexico bright spots are low impedance sands and are characterized by a high negative normal incidence reflection (AVO intercept) and a negative gradient, thus giving a positive A*B attribute.

The basic goal in this study was to propose and test an effective AVA muting algorithm that could be used with interpreted data as an aid to identify sands that fall into the Class III

---

[1] **email:** doug@sep.stanford.edu

AVO category. Also some basic AVA theory and the effectiveness of AVA as a hydrocarbon indicator will be discussed.

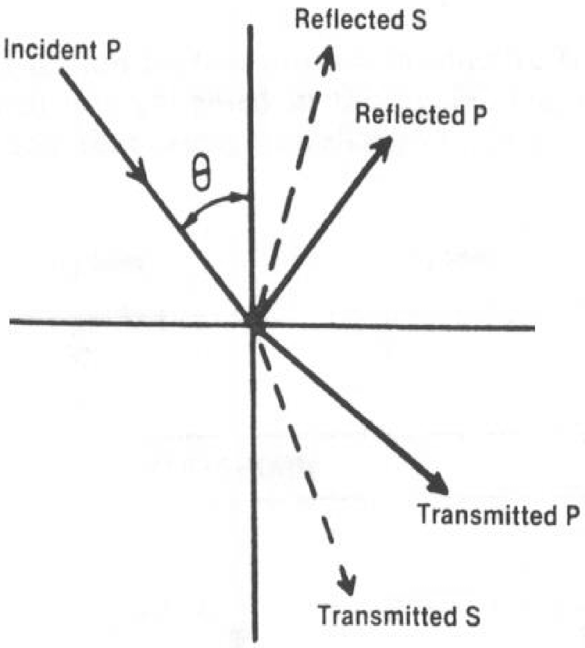

Figure 1: Theoretical energy partition at an interface. doug1-inter [NR]

AVO THEORY

Basic AVO theory is well understood because it is widely used as a tool in hydrocarbon detection (Smith, 1987). We will highlight a few of the most important ideas to keep in mind when doing AVA analysis. Figure 1 shows the theoretical energy partition at an interface. This figure illustrates an important point that accounts for AVA phenomena: the conversion of P-wave energy to S-wave energy. Though the majority of seismic data is recorded simply as a single component pressure wave, the fact that the Earth is elastic causes amplitudes of P-wave arrivals to be a function of S-wave properties of the rocks. In theory, the best AVA attribute would be one that included the S-wave reflection coefficient (R_s) (Castagna and Smith, 1994). In practice, R_s is tricky to obtain and the P-wave reflection coefficient (R_p) is what we have in the vast majority of cases (Smith and Sutherland, 1996).

Classification of AVO sands was first done by Rutherford and Williams (1989). Though a greater number of AVO signatures have now been classified, we will focus on only the typical Gulf of Mexico bright spot (Class III). This anomaly is caused by a relatively low impedance oil or gas bearing sand that shows up as a high amplitude anomaly on far offset sections. Figure 2 shows the cause of this: a high negative reflection coefficient (intercept, A) and a negative gradient, B. In the cases of deeper targets or on-shore facies, the hydrocarbon bearing

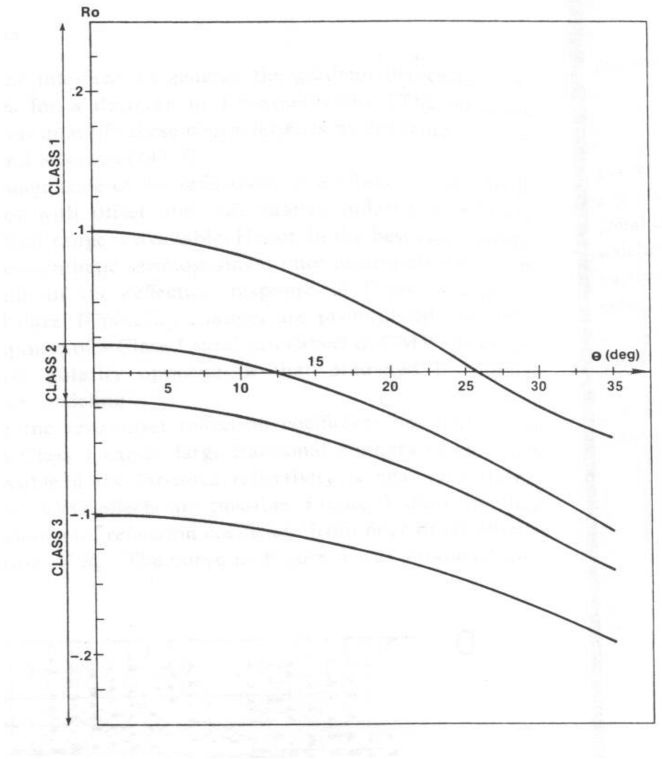

Figure 2: AVO classifications. doug1-type [NR]

sands might be high impedance, and thus the dim spot associated with Class I AVO sands would be of interest (Mavko, 2000).

The formulas for A and B up to a 30^o incidence angle are described by Shuey (1985) as approximations of the Zoeppritz equations:

$$R(\theta) \approx A + B\sin^2\theta \tag{1}$$

with

$$A = \left(\frac{\Delta Vp}{Vp} + \frac{\Delta\rho}{\rho}\right)/2 \tag{2}$$

and

$$B = -2\frac{{V_s}^2}{{V_p}^2}\frac{\Delta\rho}{\rho} + \frac{\Delta V_p}{2V_p} - 4\frac{{V_s}^2}{{V_p}^2}\frac{\Delta V_s}{V_s}\,, \tag{3}$$

where V_p, V_s, ρ are the average across an interface, that is $\frac{X_1+X_2}{2}$, and $\Delta V_p, \Delta V_s, \Delta\rho$ are the difference across an interface, that is $X_2 - X_1$. Past 30^o these approximations break down, and thus we must be careful to limit our maximum offset ray parameter to the value corresponding to an incidence angle of 30^o.

MIGRATION / IMAGE GATHER EXTRACTION

The migration program used in this project was developed by Biondi. It uses a variation of the split-step method (Stoffa et al., 1990) with the Double Square Root (DSR) equation (Claerbout, 1985). So for each depth step wave-fields at different reference velocities are generated, then an interpolation in the space domain is used as needed. For this study, three reference velocities were used. By using the split-step with the DSR, Biondi's algorithm is very effective in positioning reflectors correctly, even in regions of sharp velocity contrast, such as sediment in contact with salt (Claerbout, 1985).

The extraction of angle gathers using this migration algorithm is relatively straight forward. After the wave-field has been downward continued, a slant stack is applied before imaging (Biondi, 2000):

$$D(\omega,\mathbf{m},x_h;z=0) \overset{DSR}{\Longrightarrow} D(\omega,\mathbf{m},x_h;z) \tag{4}$$

$$D(\omega,\mathbf{m},x_h;z) \overset{SlantStack}{\Longrightarrow} D(\omega,\mathbf{m},P_h;z) \tag{5}$$

$$D(\omega,\mathbf{m},P_h;z) \overset{Imaging}{\Longrightarrow} D(t=0,\mathbf{m},P_h;z)\,. \tag{6}$$

In order to ensure true amplitudes in the image, migration was done as in my other paper in this report (Gratwick, 2001). Amplitude weighting was applied according to Sava and Biondi (2001). Angle gathers are subsets of $D(t=0,\mathbf{m},P_h;z)$ with the midpoint constant (Biondi, 2000). The angle gathers are actually not exactly a function of angle. Instead they are a function of offset ray parameter (P_h). Offset ray parameter and angle are related by equation (7):

$$\frac{\delta t}{\delta h} = P_h = \frac{2\sin\theta\cos\phi}{V(z,\mathbf{m})}. \tag{7}$$

In equation (7), θ is the incident angle, ϕ is the geologic dip, and $V(z,\mathbf{m})$ is the velocity function. Thus, if the geology is relatively flat and the velocity function can be well approximated, incidence angle is a simple function of offset ray parameter.

AVA ANALYSIS ALGORITHM

The AVA analysis performed in this study is done using AVA cross-plotting (Castagna and Swan, 1997). There are a number of sources that document this technique as being effective to find Class III AVO sands (low impedance), and a technique described by Ross is the model for our algorithm (Ross, 2000). The basic outline of this technique involves the plotting of each image point on an A vs. B grid, then zeroing points in the cross-plot, leaving only points of high A*B values.

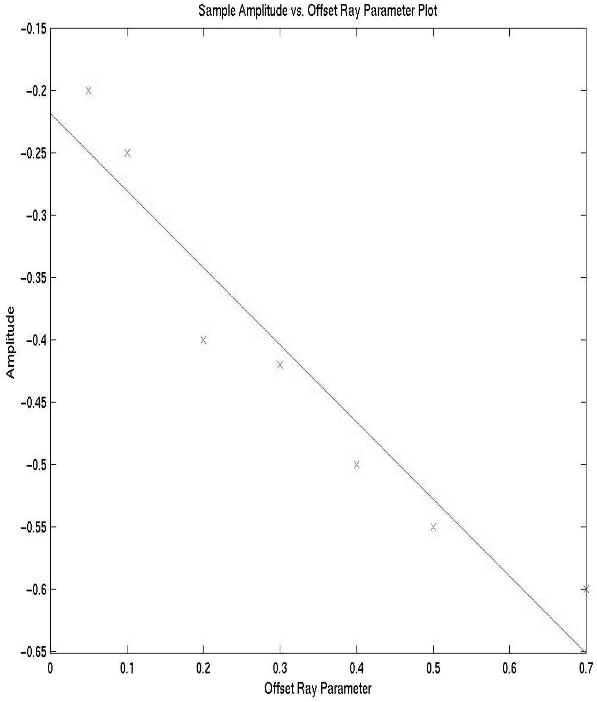

Figure 3: Typical amplitude plot for Class III AVO sand. Line is least-squares fit. Y-intercept of line is A (AVO intercept), slope of line is B (AVO gradient). doug1-amp [NR]

Extracting A and B

In order to extract A and B values from the image, it must be assumed that the reflectors in the angle gathers are flat. This is because the algorithm takes amplitude values from horizontal lines on the image gathers. Getting image gathers flat is trivial for synthetic data, since the velocity function is known. For real data, getting image gathers flat is a product of good velocity analysis (Yilmaz, 1987). In practice, often we use the envelope of a trace, rather than the amplitude. This way, events do not need to be exactly flat. For our study, the gain in resolution of the A*B image justified using amplitude instead of envelope.

Since we don't want points in the image gather that correspond to values outside the range of our maximum P_h, a mute is applied to zero irrelevant parts of the image gathers (Gratwick, 2001). Figure 3 shows a hypothetical amplitude vs. offset ray parameter plot for a reflector from a Class III AVO interface. There is a simple least-squares fit to these points (zeroed amplitude values are not included), and the y-intercept of this line is the AVO intercept (A). The slope of this least-squares line is the AVO gradient (B). Thus from the image gathers, two panels are created: one for the intercept and another for the gradient.

Cross-plot Muting

A scatter-plot of A vs. B from the synthetic data image used in this study is seen in Figure 4. There is a noticeable clustering of points in the middle of the plot. These correspond to the

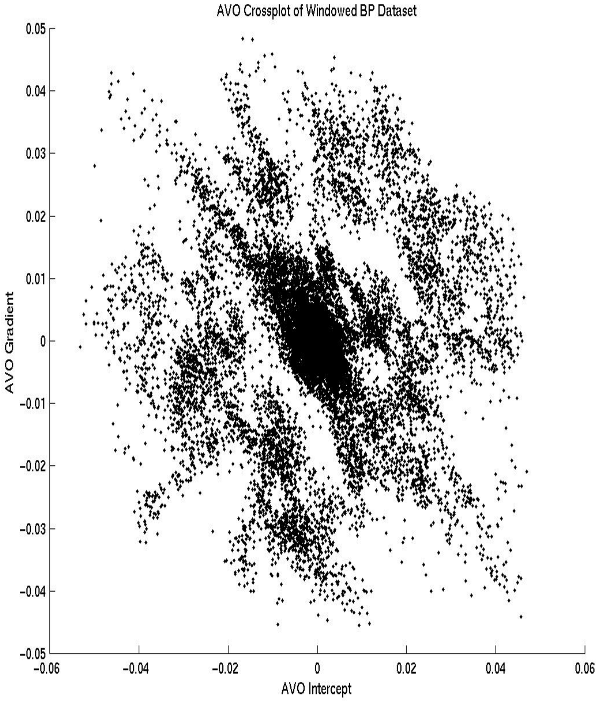

Figure 4: A vs. B scatter-plot (from synthetic image used in this study). doug1-plot1 [NR]

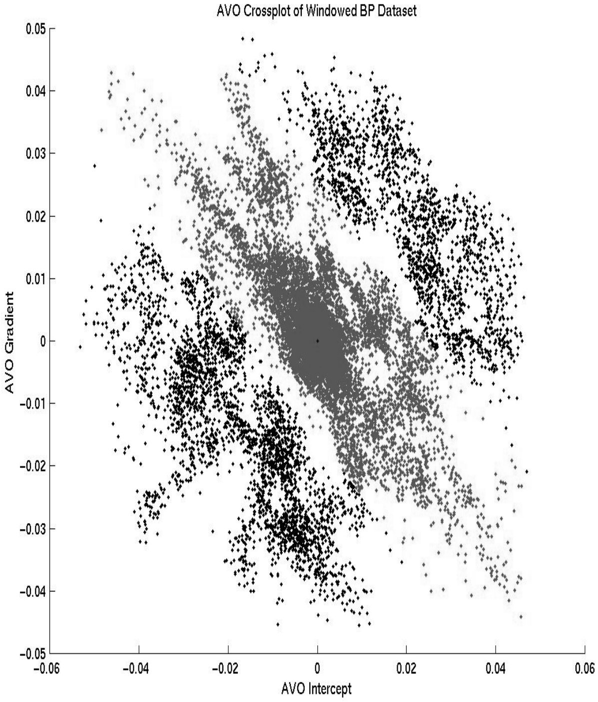

Figure 5: A vs. B scatter-plot with mute fairway defined. doug1-plot2 [NR]

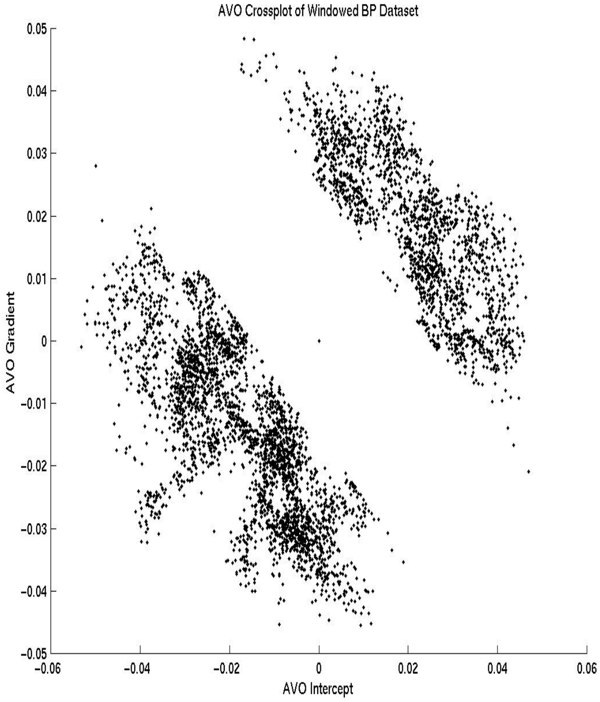

Figure 6: A vs. B scatter-plot with mute fairway zeroed, leaving points of image corresponding to a Class III anomaly. doug1-plot3 [NR]

background values, or those parts of the image that are not associated with a Class III anomaly. The points farthest from the origin in quadrants I (upper-right) and III (lower-left) are parts of the image that are associated with a Class III anomaly. Thus, a mute fairway can be defined where values in the fairway are regarded as background parts of the image (Figure 5). These values are muted, and we are left with a scatter-plot of points where a Class III AVO anomaly is detected (Figure 6). When transformed back into two panels (A and B) and multiplied together (A*B), the resultant image has energy only at areas associated with an interpreted Class III AVO anomaly.

SYNTHETIC DATA EXAMPLE

The elastic synthetic data used for this study is provided by BP (Gratwick, 2000). A benefit of using the synthetic is that we know the density, S-wave velocity, and P-wave velocity functions used to create the data. These three parameters can give both an AVO intercept (A) panel and AVO gradient (B) panel, using equations (1), (2), and (3). Multiplying the two panels together gives the expected A*B response of the migrated image (Figure 7). Areas of the model that have a Class III anomaly should show up as the same color (white) in the image and at the same locations.

The initial (no mute) A*B of the image is seen in Figure 8. Overall, the image is comparable to the model but there are two notable problems:

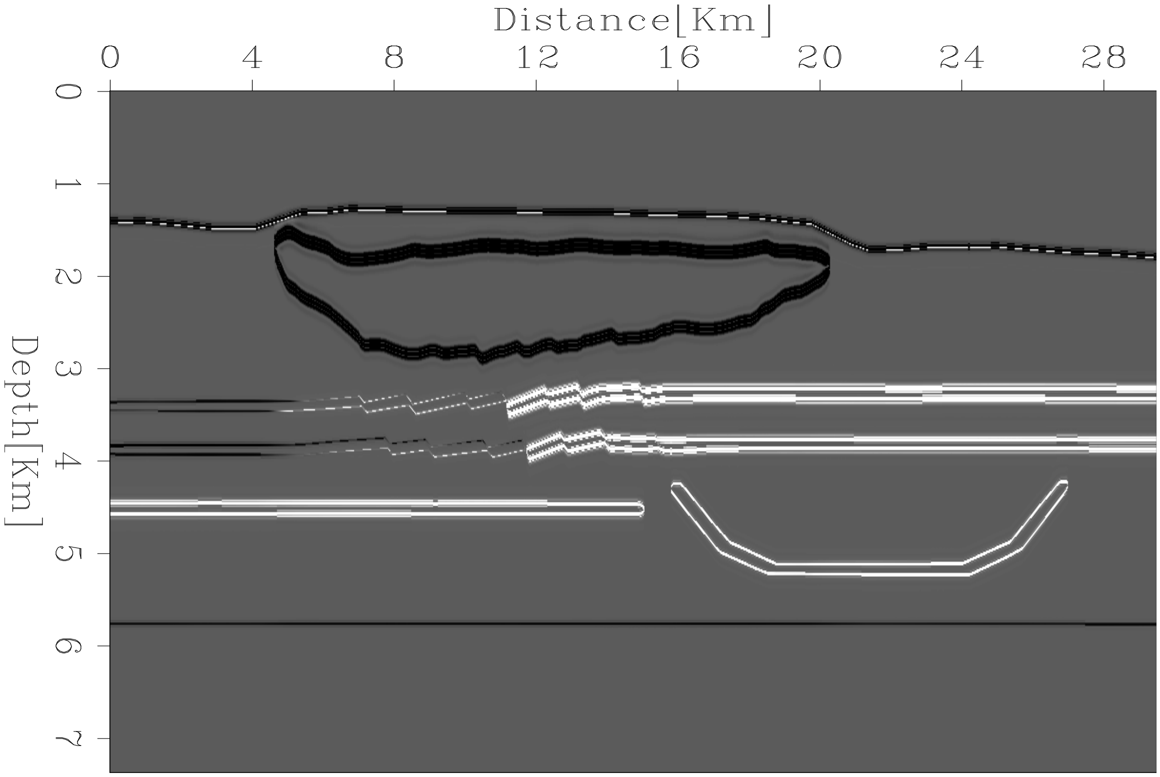

Figure 7: A*B model from $V_p, V_s, and \rho$ models. (Note: white denotes high A*B value, or Class III AVO anomaly) The model has a salt body (2-3 km depth, 4-20 km distance) and a channel structure (4-5 km depth, 16-28 km distance). doug1-AB_model [ER]

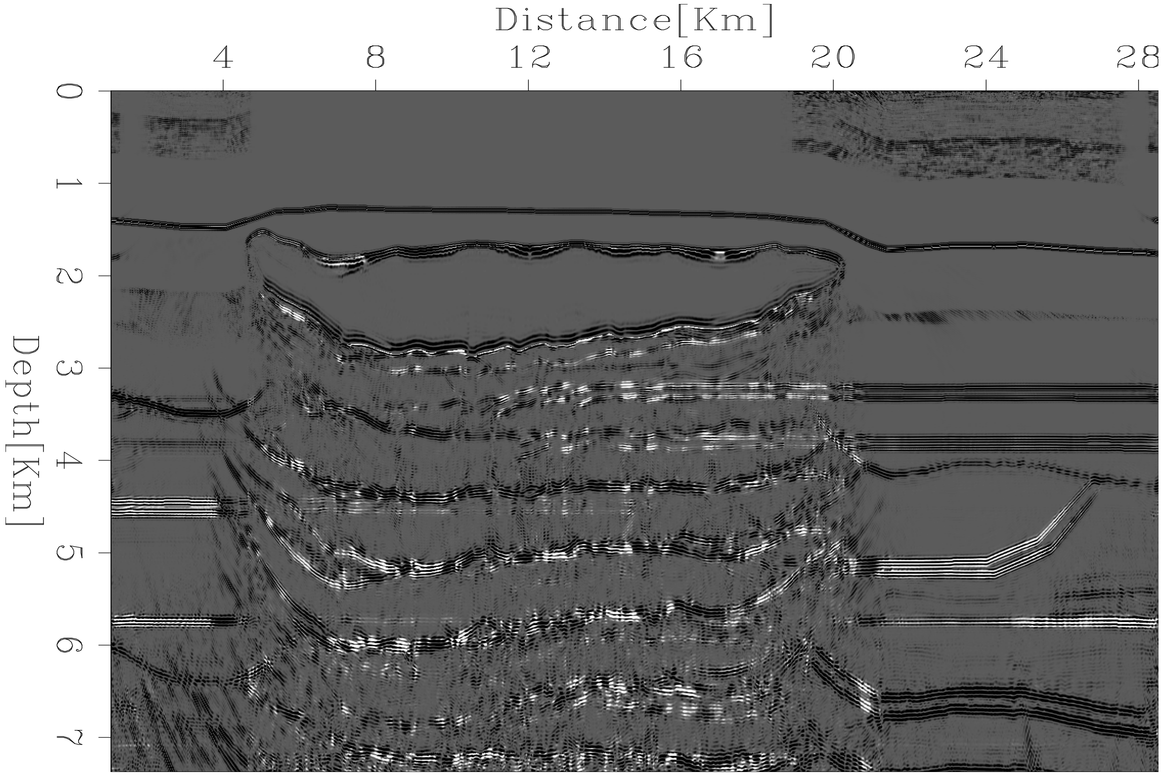

Figure 8: Original A*B Extracted from angle gathers (no mute). doug1-AB_data_orig [ER]

1. Areas of poor illumination; specifically on the left side of the channel structure and under the salt. In these areas there is not enough energy from the wave-field to detect AVA effects.

2. Multiples corrupting the primary signal. The interference occurs at different offset ray parameter, different parts of the image, and can cause the least-squares line fit to be incorrect because of anomalous amplitude points. This is most evident in the sand lens at 4.5 km depth under the salt.

To account for the problems with the low energy, the AVA muting algorithm described in the previous section was implemented. Figure 9 shows the result of the mute applied to all areas of the image at once (all image points were plotted at the same time). The hydrocarbon layers below the salt are much more clear, and even parts of the left flank of the channel can be seen easier.

To account for problems with multiple energy, a multiple suppression technique introduced by Rickett et al. (2001) was used along with the AVA mute algorithm. This technique is designed to reduce energy from surface multiples; in this case from the water bottom and from the top and bottom of the salt. The multiple suppression worked well to resolve the sand lens at 4.5 km under the salt, but still internal salt multiples corrupted events near the base of the salt (Figure 10).

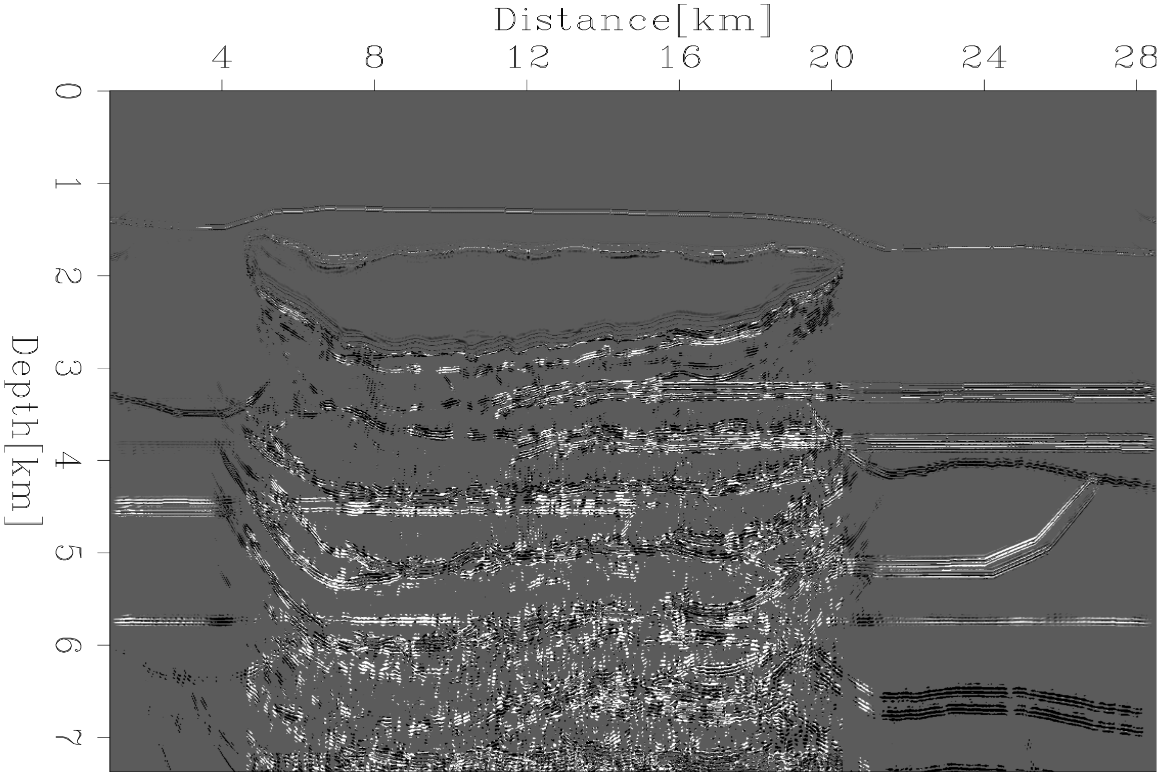

Figure 9: A*B after AVA mute algorithm doug1-AxB_data_orig [ER]

REAL DATA EXAMPLE

The real data used in this study were provided by WesternGeco. The synthetic model used in the previous section was modeled after this real dataset. Thus many of the imaging problems faced in the synthetic data presented themselves in the real data. Since we had a rough idea of the subsurface geology, the velocity analysis was relatively easy. The actual geology and synthetic model are likely very different, but the size and shape of the salt body is fairly uniform between the two, and the velocity gradients are comparable. Figure 11 shows extracted image gathers from both outside and under the salt. We can see that the events are relatively flat, so our AVA algorithm should work well. Figure 12 shows the stack of the angle gathers. There are a few notable bright spots around the right side of the salt and closer to the bottom of the salt that may correspond to hydrocarbons.

The A*B image of the WesternGeco data is shown in Figure 13, and the image after the AVA muting algorithm is show in Figure 14. Overall, the AVA algorithm seems to have worked well, with the A*B image confirming that the bright spots in the stacked image could very well be reflections from a low impedance gas or oil sand. Similar to the synthetic image, the algorithm helps to illuminate reflectors under the salt. However, the real data image seems to have even less energy under the salt. This is expected since the wavefield in the real data undergoes a lot more scattering than in the synthetic model.

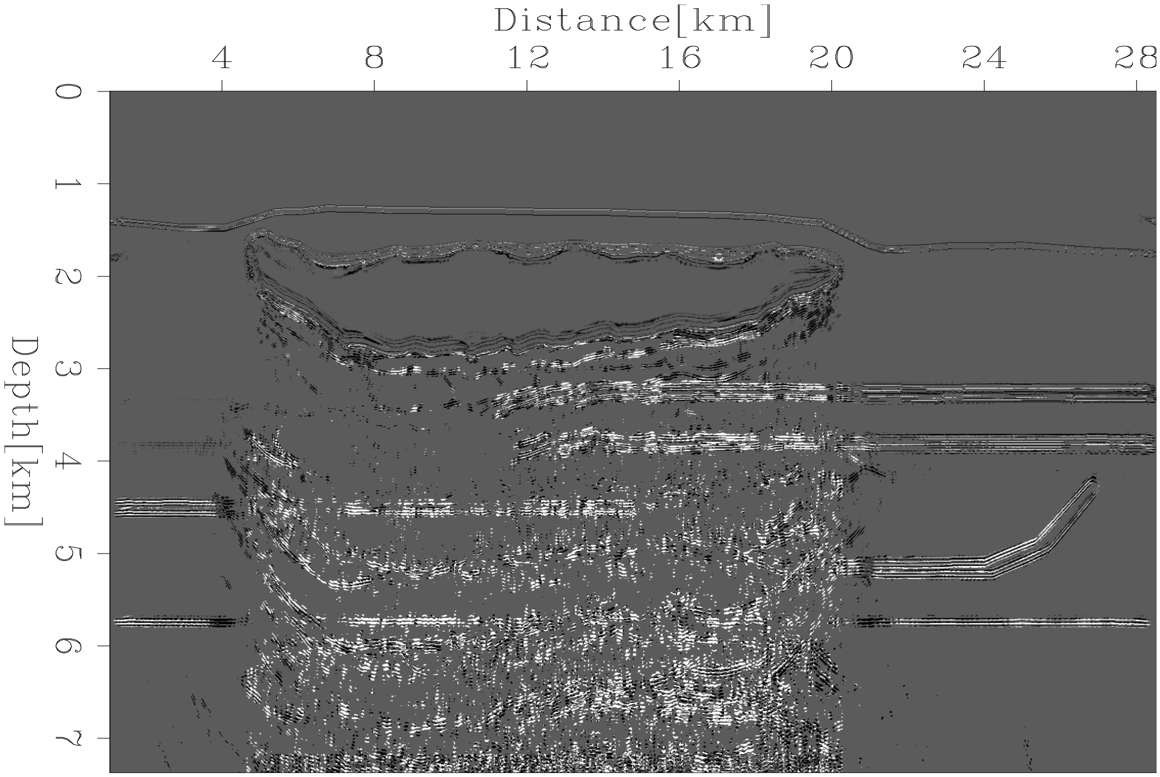

Figure 10: A*B after Rickett multiple suppression and the AVA mute algorithm doug1-AxB_data_rickett [ER]

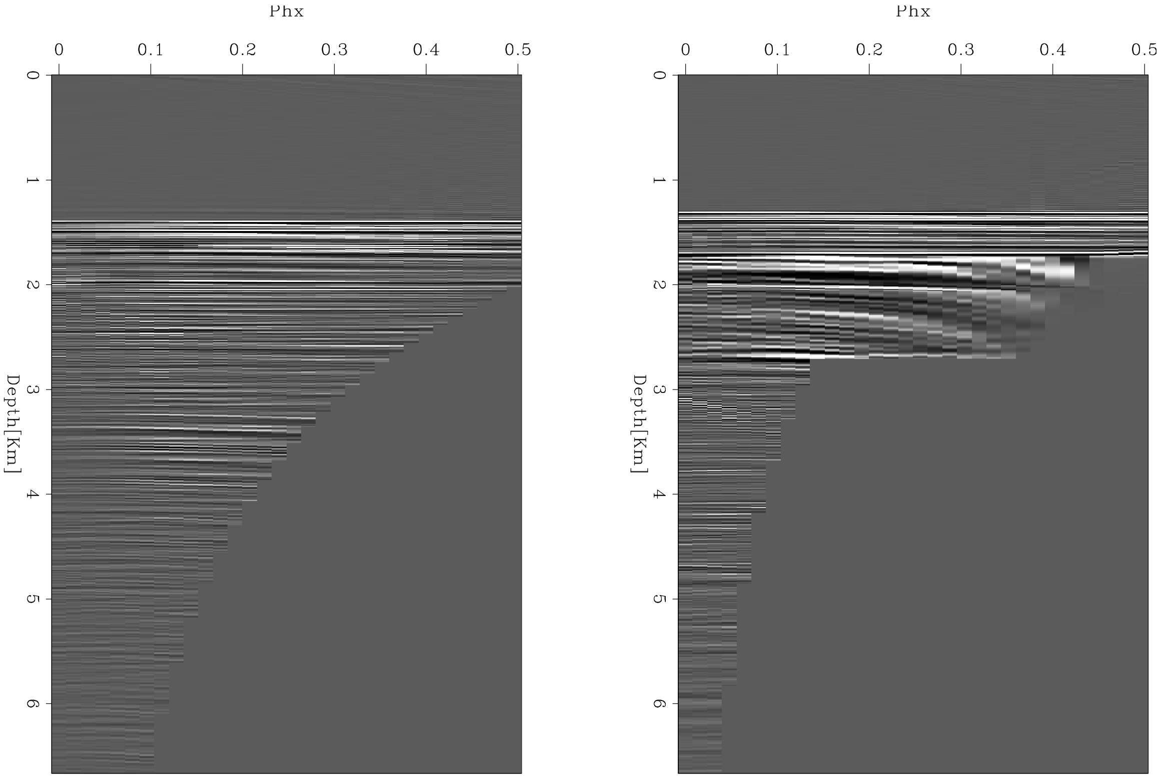

Figure 11: Angle gather from outside the salt (left) and in the salt (right). doug1-gulf_ig [ER]

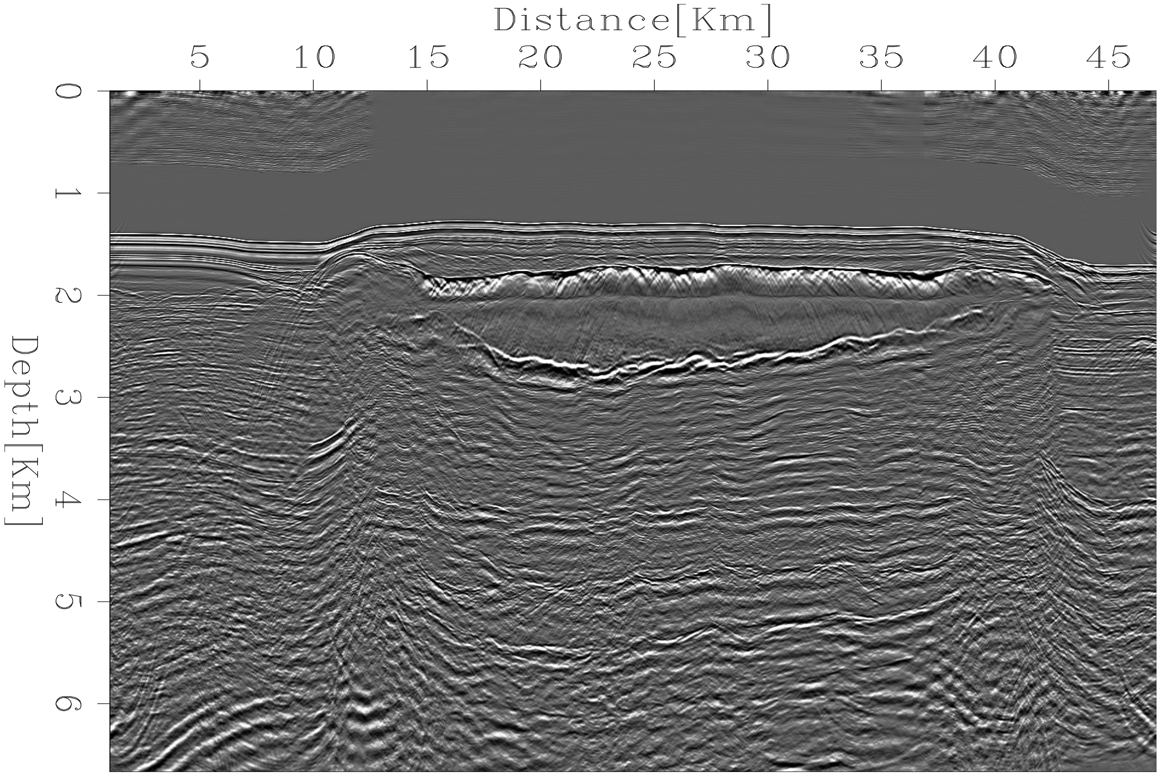

Figure 12: Image obtained from stacking angle gathers. doug1-gulf_stack [ER]

CONCLUSION

The goal in this study was to create and implement an AVA analysis algorithm that effectively identified Class III AVO sands. From the synthetic and real data cases, it is clear that our algorithm can select parts of the image corresponding to Class III AVO anomalies. However, it is also clear that a multiple suppression technique must be used in order to make our AVA algorithm effective in complex settings. Even then, the scattering effect of sharp velocity contrasts can inhibit good AVA analysis.

It is important to realize that seismic attributes, such as amplitude, hold a lot of information about rock properties. However, amplitudes can be altered significantly throughout the course of seismic processing. With this in mind, AVA data should be used carefully, as an aid to interpretation, rather than a direct hydrocarbon indicator.

ACKNOWLEDGMENTS

We would like to thank WesternGeco for the rights to use and publish the real dataset used in this paper.

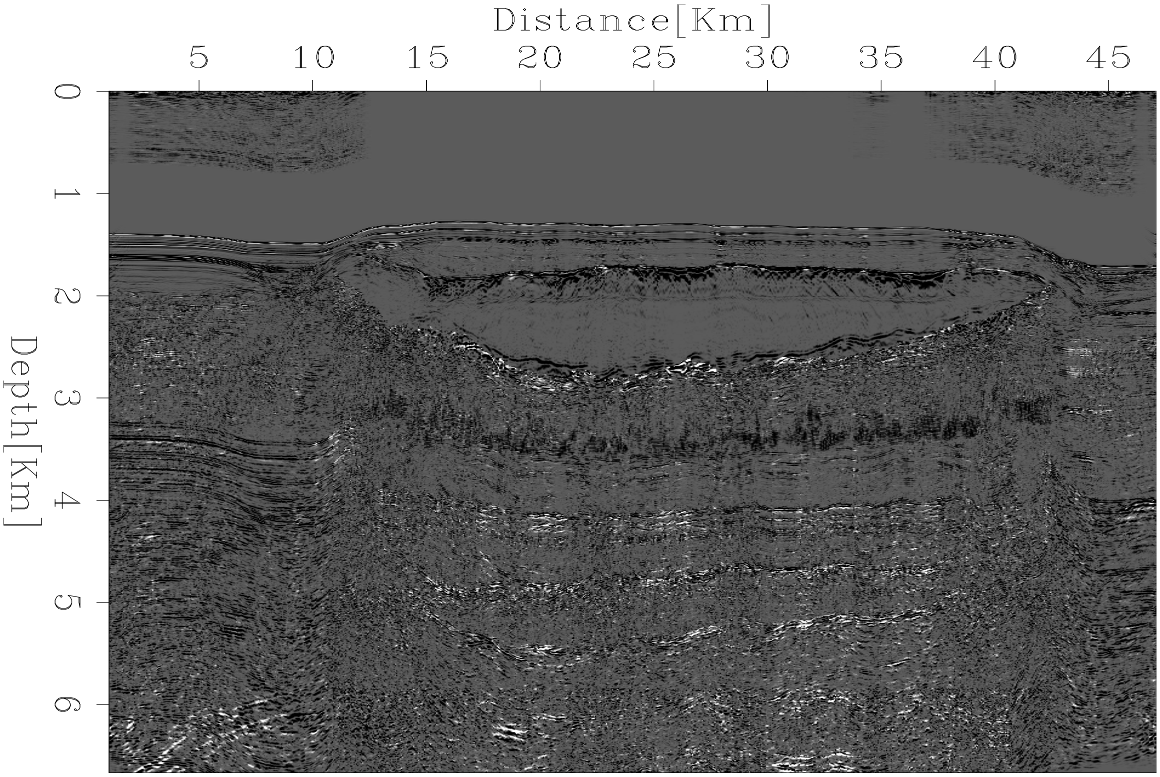

Figure 13: Original A*B image showing some bright spots under right margin of salt at about 43 km. doug1-gulf_AB [ER]

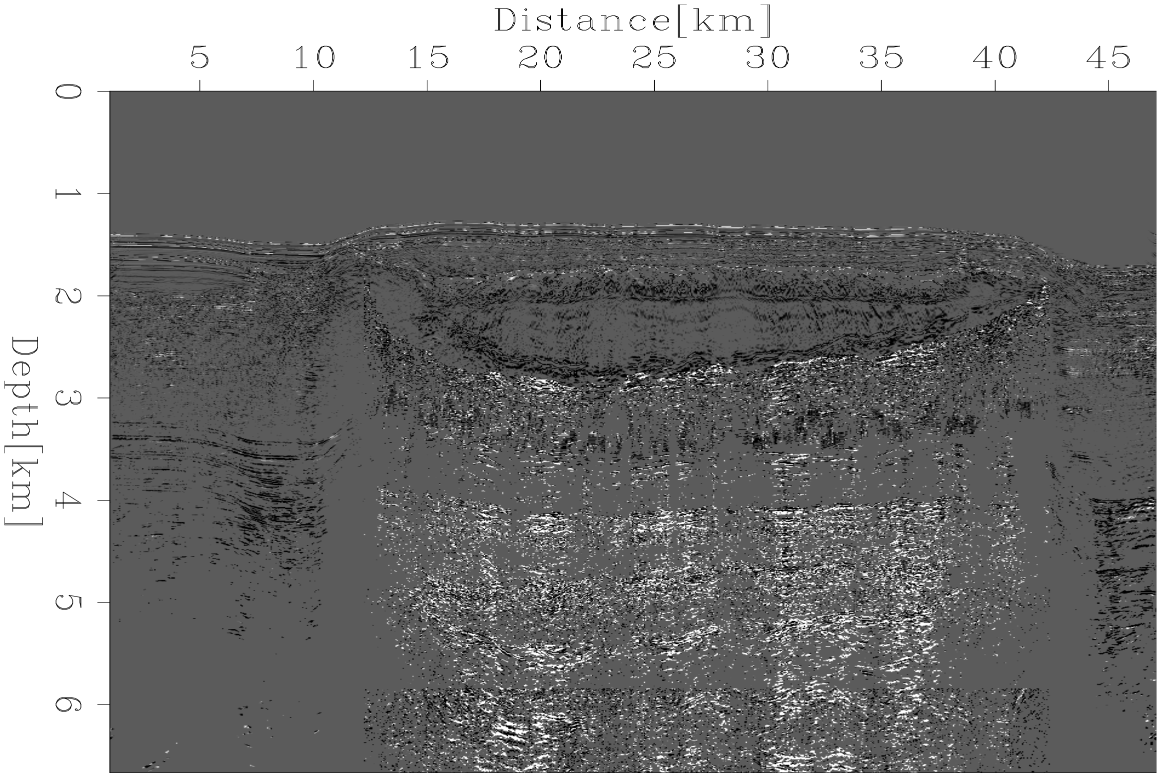

Figure 14: A*B after mute algorithm, isolating the bright spots of the previous figure (especially directly below salt). doug1-AxB_data_gulf [ER]

REFERENCES

Biondi, B., 2000, 3-D Seismic Imaging: Class notes, `http://sepwww.stanford.edu/sep/prof/index.html`.

Castagna, J. P., and Smith, S. W., 1994, Comparison of AVO indicators: A modeling study: Geophysics, **59**, no. 12, 1849–1855.

Castagna, J. P., and Swan, H. W., 1997, Principles of AVO crossplotting: AAPG Mid-Continent Section Meeting; Abstracts; AAPG Bulletin, **81**, no. 8, 1348.

Castagna, J. P., Swan, H. W., and Foster, D. J., 1998, Framework for AVO gradient and intercept interpretation: Geophysics, **63**, no. 3, 948–956.

Claerbout, J. F., 1985, Imaging the Earth's Interior: Blackwell Scientific Publications.

Gratwick, D., 2000, Subsalt imaging of a 2-D elastic synthetic model, using prestack, split-step, wave equation migration: SEP–**103**, 169–181.

Gratwick, D., 2001, The accuracy of wave-equation migration amplitudes: SEP–**108**, 63–72.

Mavko, G., 2000, GP262 Rock Physics Spring 2000: Course Reader.

Prucha, M., Biondi, B., and Symes, W., 1999, Angle-domain common image gathers by wave equation migration: 69th Ann. Internat. Meeting, Soc. Expl. Geophysicists, Expanded Abstracts, **1**, 824–827.

Rickett, J., Guitton, A., and Gratwick, D., 2001, Adaptive multiple subtraction with non-stationary helical shaping filters: SEP–**108**, 275–282.

Ross, C. P., 2000, Effective AVO crossplot modeling: A tutorial: Geophysics, **65**, no. 3, 700–710.

Rutherford, S. R., and Williams, R. H., 1989, Amplitude-versus-offset variations in gas sands: Geophysics, **54**, no. 6, 680–688.

Sava, P., and Biondi, B., 2001, Amplitude-preserved wave-equation migration: SEP–**108**, 1–26.

Sheriff, R., 1995, Exploration Seismology: Cambridge.

Shuey, R. T., 1985, A simplification of the Zoeppritz equations: Geophysics, **50**, no. 4, 609–614.

Smith, G. C., and Sutherland, R. A., 1996, The fluid factor as an AVO indicator: Geophysics, **61**, no. 5, 1425–1428.

Smith, G. C. e. a., 1987, Weighted stacking for rock property estimation and detection of gas: Geophysical Prospecting, **35**, no. 9, 993–1014.

Stoffa, P. L., Fokkema, J. T., de Luna Freire, R. M., and Kessinger, W. P., 1990, Split-step Fourier migration: Geophysics, **55**, no. 4, 410–421.

Yilmaz, O., 1987, Seismic Data Processing: Soc. Expl. Geophys.